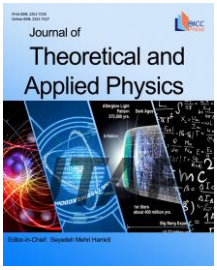

J. Theor. Appl. Phys., 2026; 20(3): 213-223

Journal of Theoretical and Applied Physics (JTAP)

https://doi.org/10.57647/jtap.2026.8615.0306

Research Article

Differential Cross-Section Analysis Using Thermal Volkov Wave Functions and Gaussian-Screened Potentials in Laser-Assisted Scattering

Dol Raj Paudel[1], Bibek Pandey[1], Madhurendra Lal Das[1], Hemant Bahadur Deuba[2], Kishori Yadav[1], Suresh Prasad Gupta[1], Saddam Husain Dhobi[1,2*]

[1]*Department of Physics, Patan Multiple Campus, Tribhuvan University, Lalitpur, Nepal*
[2]*Central Department of Physics, Tribhuvan University, Kirtipur, Kathmandu, Nepal*

***Corresponding author:** saddam@ran.edu.np

Article History:

Received:
22 August 2025

Revised:
22 September 2025

Accepted:
17 October 2025

Published Online:
07 January 2026

Published in Issue:
30 June 2026

Abstract

The aim of this work is to study the scattering behavior of electrons in a Gaussian-screened potential under polarized laser fields (linear, circular, and elliptical) within thermal and nonthermal environments. For this purpose, we developed a theoretical model using the thermal Volkov wave function to describe electron dynamics in the Gaussian-screened potential. Using the thermal Volkov wave function, we derived the scattering and transition matrices via the Kroll-Watson approximation. From the transition matrix, the differential cross-section was obtained, which directly characterizes the scattering behavior of electrons in the Gaussian-screened potential. The developed differential cross-section model was computed to analyze electron behavior under thermal and nonthermal conditions. Observations indicate that the differential cross-section is highest for elliptical polarization, followed by circular and linear polarizations. Additionally, the differential cross-section is greater in thermal environments compared to nonthermal ones. Also, the screening parameters significantly affect resonance positions and differential cross section magnitudes, shifting peaks toward smaller angles and increasing cross-section values at higher screening. Distance separation studies reveal contrasting trends between thermal and non-thermal regimes, and photon energy variations highlight polarization reversals at higher energies. The study demonstrates that differential cross section can be effectively manipulated by tuning polarization, screening, temperature, and scattering angle. This study shows that electron scattering with Gaussian-screened potentials can be controlled by tuning polarization, screening, temperature, and scattering angle, which has practical applications in plasma physics, fusion energy, and semiconductor technology. The findings also provide insights for advanced material processing, space plasma modeling, and the development of laser-based diagnostic tools.

Keywords: Scattering, Gaussian-screened potential, Polarization, Thermal and nonthermal effect, Differential cross section, Thermal Volkov wave functions

Cite this article: Paudel, D., Pandey, B., Lal das, M., Deuba, H. B., Yadav, K., Prasad Gupta, S., Dhobi, S. H. (2026). Differential Cross-Section Analysis Using Thermal Volkov Wave Functions and Gaussian-Screened Potentials in Laser-Assisted Scattering. *J. Theor. Appl. Phys.,* 20(3), 213-223. https://doi.org/10.57647/jtap.2026.8615.0306

1. Introduction

Quantum dots (QDs) are nanostructures with unique optical and electrical properties due to quantum confinement, which allows for precise tuning of these properties based on size and composition. Since their discovery in the 1980s, QDs have been widely researched for their applications in photonics, including solar cells, electroluminescence, photon imaging, and nonlinear optics (Yu et al., 2000). Various types of QDs, such as cadmium selenide (CdSe), Zinc sulfide (ZnS), and cadmium telluride CdTe, have been explored for both fundamental and applied sciences (Liu et al., 2009; Zou et al., 2011; Li et al., 2005). Adjusting QD size allows for customizable optical properties, opening opportunities for advanced photonic devices. Studies on two-electron QDs have provided insights into electron-electron interactions, aiding the theoretical understanding of their structure using techniques like Hartree-Fock and effective mass theory (Chakraborty, 1999; Peeters, 1990). Modifying QD confinement properties can alter photon emission frequency, highlighting their versatility in optical technologies (Bahar et al., 2018). Artificial atoms, also known as QDs, have garnered significant attention for nanoscale applications, including digital photography, optoelectronics, quantum information processing, and solar energy harvesting (Chakraborty, 1999). Their electrical and optical properties resemble real atoms, except for a scale factor and the absence of a Coulomb center potential.

QDs are typically 1–100 nm in size and contain multiple electrons in a confined space, making their interaction with ultrashort, strong radiation fields critical for understanding their electrical dynamics. Radiation within the THz and mid-IR range can excite or ionize QDs, leading to active experimental inquiry (Jacob et al., 2012). Recent experiments using ultrafast THz and mid-IR radiation have probed the femtoscale structural dynamics of QDs. Like atomic systems, these ultrafast interactions are expected to reveal valuable insights into QDs' electronic dynamics. Since early investigations, much theoretical and experimental work has focused on the correlation and entanglement of confined electrons.

Bryant (1997) conducted one of the earliest studies on electron-electron Coulombic collisions, showing how QD size influences the transition from independent particle systems to many-body systems. As QD size increases, the significance of correlation interactions grows, particularly since the Coulomb energy decreases more slowly than single-particle energy differences (Nikolopoulos and Bachau, 2016). Advances in nanofabrication have further enabled the use of QDs in optoelectronic devices, emphasizing nonlinear optical effects, refractive index changes (RICs), and absorption coefficients (ACs). The influence of external fields, especially intense laser fields (ILF), has been found to significantly alter QD properties, breaking system symmetry and enabling second harmonic generation.

Studies on laser-dressed cylindrical QDs with axial Morse potentials show that structural parameters and external fields closely impact their intraband optical properties, offering potential for optoelectronic device applications (Ungan et al., 2021).

At the nanoscale, electron movement can be restricted in various ways, forming structures like quantum wells, wires, and dots. Advances in crystal growth techniques like molecular beam epitaxy enable precise control over QD characteristics, making them valuable for semiconductor laser diodes and optoelectronic devices (Khordad, 2012; Xie, 2008).

The study of QD electron dynamics under strong laser fields has led to breakthroughs, such as attosecond laser pulse generation (Gunatilaka and Gamalath, 2016; Bauer, 2006).

The motivation for this study stems from the need to understand and control electron scattering dynamics in Gaussian-screened potentials under polarized laser fields, which has important implications for plasma physics, fusion energy, semiconductor technology, and advanced material processing.

Despite extensive research on quantum dot and electron dynamics, comprehensive theoretical models that simultaneously account for polarization effects, thermal and non-thermal environments, screening parameters, and scattering angles remain limited. This work addresses this gap by developing a differential cross-section model based on thermal Volkov wave functions and the Kroll–Watson approximation.

Using this framework, we derive the scattering and transition matrices necessary to evaluate the differential cross section (DCS) and systematically analyze how polarization, screening, temperature, and scattering angle collectively influence electron behavior.

This theoretical approach not only advances the fundamental understanding of laser-assisted electron scattering but also provides practical insights for experimental applications and technological developments in plasma physics, fusion energy, semiconductor technology, and laser-based diagnostics.

2. Materials and methods

The lateral coupling quantum well wires are to be exposed to a monochromatic planar wave of frequency in a strong terahertz laser field. The laser beam is polarized in a linear manner along the x-axis direction and non-resonant with

10.57647/jtap.2026.8615.0306

the laterally-coupled quantum well wires (LCQWWs). As a result, the electron's transverse motion is the only thing that the laser field alters; its axial motion remains unchanged.

The time-dependent Schrödinger equation can be used to describe the conduction-band electrons dynamics of the LCQWWs in the (x, y) plane:

$$\left[\frac{1}{2m^*}\left(p-\frac{e}{c}A(t)\right)^2+V\right]\psi(x,y,t)=i\hbar\frac{\partial\psi(x,y,t)}{\partial t} \quad (1)$$

where m^* represents the conduction-band electronic effective mass, p represents the momentum within the (x, y) plane, e represents the electron charge, c represents the speed that light travels in vacuum, and $\hbar$ is the Planck constant.

The vector potential that defines the laser field is expressed as $A(t) = A_0\cos\omega t$, where A_0 is the amplitude of wavefunction of laser photons.

The Kramers-Henneberger unitary transform and the dipole approximation can be used to further modify Eq. (1) (Liu et al., 2009).

$$\left[-\frac{\hbar^2\nabla^2}{2m^*}+\hat{V}\right]\hat{\psi}(x,y,t)=i\hbar\frac{\partial\hat{\psi}(x,y,t)}{\partial t} \quad (2)$$

where $\hat{\psi}(x,y,t)$ represents the wave function and $\hat{V}(x, y, t) = V(x + \alpha_0\sin(\omega_d t), y)$ represents the laser-dressed confining potential. The quiver motion of a single electron in the laser field is described by the laser-dressed variable α_0.With a period of $T = 2\pi/\omega_d$, $\hat{V}(x, y, t)$ represents a periodical function of time that oscillates at frequency ω_d. It is assumed that τ denotes the electron's characteristic transit time within the quantum structure.

The Schrodinger equation in dependence on time to obtain the wave form of an electron connected to an external electromagnetic field.

The laser field can be represented by the vector potential A(t) in the dipole approximation. Consequently, an electron connected to an external field of electromagnetic radiation (Kim, 2022 and Bransden and Joachain, 2003) has time-dependent wave function is:

$$X(r,t)=\frac{1}{(2\pi)^{3/2}}exp\left\{i\frac{p}{h}.\left(r+\frac{e}{m}\int A(t)dt\right)\right.$$
$$\left.-i\frac{E}{\hbar}t-i\frac{e^2}{2m\hbar}\int A^2(t)\right\}dt \quad (3)$$

This goes by the name of the Volkov wave function. E is the free electron's kinetic energy. Similarly for elliptical polarization, we also have vector potential (Yadav et al., 2020) we have $A=a\left[\hat{x}\cos(\omega t)+\hat{y}\sin(\omega t)\tan\left(\frac{\xi}{2}\right)\right]$ and then for this we have Volkov wave function in thermal case form (Dhobi et al., 2025a; Dhobi et al., 2024) we have

$$X_E(r,t)=\frac{1}{(2\pi)^{3/2}}exp\left\{i\frac{p}{h}.r+R\sin(\omega t-\gamma)\right.$$
$$-i\frac{E}{\hbar}t+i\frac{e^2a^2}{8\omega m\hbar}\left[-2\left(tan^2\left(\frac{\xi}{2}\right)+1\right)\omega t\right.$$
$$+\left(tan^2\left(\frac{\xi}{2}\right)-1\right)sin(2\omega t)$$
$$\left.\left.+2\,tan^2\left(\frac{\xi}{2}\right)cos(2\omega t)\right]\right\}-k_e\nabla\mathrm{Texp(i}\omega_{eT}\mathrm{t)} \quad (4)$$

Form Eq. (4), ξ is ellipticity and $-k_e\nabla\mathrm{Texp(i}\omega_{eT}\mathrm{t)}$ term is thermal wave function, where k_e is electron thermal conductivity, ∇T is change in temperature of electron, ω_{eT} is frequency of thermal electron (electron in thermal environment) (González De La Cruz, G., & Gurevich, 1996).

Now to obtained DCS with Kroll Watson Approximation for Linear Polarized (Kroll and Watson, 1973) we have,

$$S_{fi}=\delta_{fi}-\frac{i}{\hbar}\int_{-\infty}^{+\infty}\langle X_f(r,t)\,|V(r)|\,X_i(r,t)\rangle dt \quad (5)$$

Now substituting value of $X_i(r,t)$ and $X_f(r,t)$ from above Eq. (4) and modified of $V(r)=-V_0J\left(\frac{2a_0r}{r_0^2}\right)\exp\left[-\frac{(r^2+a_0^2)}{r_0^2}\right]$ (Durak and Sakiroglu, 2023). We modified the potential assuming the electron is surrounding the Gaussian potential so it is geos to be multiplies by screening part and become $=-V_0J\left(\frac{2a_0r}{r_0^2}\right)\exp\left[-\frac{(r^2+a_0^2)}{r_0^2}\right]e^{-\eta r}$ here η is screening parameters. For linear polarization $\xi=0$, for elliptical polarization $\xi=\pm\pi$ and for circular polarization $\xi=\frac{\pi}{2}$ from Eq. (5). Scattering matrix (S-matrix) is a element of time development operator between unperturbed asymptotic in and out state when times tends to $-\infty\ to+\infty$ where as transition matrix in a fixed time.

Due to the application of quantum scattering theory combined with a classical treatment of the electromagnetic field, the model is regarded as semiclassical.

Equation is used in a derivation akin to that presented by (Kroll and Watson, 1973).

$$S_{fi}=\delta_{fi-\frac{i}{\hbar}}\int_{-\infty}^{+\infty}\langle X_f(r,t)|V(r)|X_i(r,t)\rangle\,dt \quad (6)$$

Eq. (6) is S-matrix represented which is combined form of Kronecker delta and transition matrix. Since we are interested to study the differential cross section (DCS) and transition matrix (T-matrix) is directly realted so from Eq. (6) we take second term which is known as transition matrix is expressed as:

$$T_{fi} = \frac{i}{\hbar}\int_{-\infty}^{+\infty} \langle X_f(r,t)|V(r)|X_i(r,t)\rangle\, dt \tag{7}$$

Eq. (7) is known as T-matrix, where, X_f and X_i *is* final and initial wave function of after and before scattering in thermal environment. To evaluate the T-matrix putting the value of Eq. (4) of Volkov thermal wavefunction and modified Gaussian-screening potential and solving with separation of algebraic term we have

$$T_{fi} = \int_{\infty}^{\infty}\int V(r)d^3r\frac{1}{(2\pi)^3}$$

$$exp\,\{ip.r\ + 2R\sin(\omega t-\gamma) - iEt\,\}dt$$

$$-\int_{\infty}^{\infty}\int V(r)d^3r\frac{k_e\nabla T_{eTi}\exp(i\omega_{eTi}t)}{(2\pi)^{3/2}}$$

$$exp\left\{-i\frac{p_f}{h}.r\ + R\sin(\omega t-\gamma) + i\frac{E_f}{\hbar}t\right\}dt \tag{8}$$

$$-\int_{\infty}^{\infty}\int V(r)\,d^3r\frac{k_e\nabla T_{eTf}\exp(-i\omega_{eTf}t)}{(2\pi)^{3/2}}$$

$$exp\left\{i\frac{p_i}{h}.r\ + R\sin(\omega t-\gamma) - i\frac{E_i}{\hbar}t\right\}dt$$

$$-\int_{\infty}^{\infty}\int V(r)\,k_e^2\nabla T_{eTi}\nabla T_{eTf}\exp(i\omega_{eT}t)dtd^3r$$

In Eq. (8) ∇T_{eTi} is change in temperature of thermal environment before scattering and ∇T_{eTf} is change in temperature of thermal environment after scattering, ω_{eTi} is the frequency of thermal electron before scattering and ω_{eTi} is energy of electron after scattering. This Eq. (8) is used to calculate the T-matrix with integration of 'r' and 't'. Also, the phase γ is defined as $\gamma = \tan^{-1}\left(tan\theta\tan\left(\frac{\xi}{2}\right)\right)$, where θ is scattering angle and γ determine the polarization case (linear, elliptical and circular) dependent on scattering angle and ellipticity. On solving Eq. (8) we get,

$$T_{fi} = -\sum_{n=-\infty} J_n(2R)\,e^{-in\gamma}2\pi\delta$$

$$(n\omega - E)\left(\frac{V_0}{(2\pi)^2 ip}\right)\frac{r_0^2}{2}$$

$$\left[1+\frac{(-\eta+ip-ipcos\theta)r_0}{2}\sqrt{\pi}e^{\frac{(-\eta+ip-ipcos\theta)^2r_0^2}{4}}\right. \tag{9}$$

$$\left.erfc\left(-\frac{(-\eta+ip-ipcos\theta)r_0}{2}\right)\right]$$

$$+\frac{k_e\nabla Te}{(2\pi)^{3/2}}\sum_{n=-\infty}^{\infty} J_n(R)\,e^{-in\gamma}2\pi\delta\left(E_f+\omega_{eTi}+n\omega\right)$$

$$\left(\frac{V_0}{(2\pi)^2 ip_f}\right)\frac{r_0^2}{2}\left[1+\frac{(-\eta+ip_f-ip_fcos\theta)r_0}{2}\right.$$

$$\sqrt{\pi}e^{\frac{(-\eta+ip_f-ip_fcos\theta)^2r_0^2}{4}}$$

$$\left.erfc\left(-\frac{(-\eta+ip_f-ip_fcos\theta)r_0}{2}\right)\right]$$

$$+\frac{k_e\nabla T_{eTf}}{(2\pi)^{3/2}}\sum_{n=-\infty}^{\infty} J_n(R)\,e^{-in\gamma}2\pi\delta\left(E_i-\omega_{eTf}+n\omega\right)$$

$$\left(\frac{V_0}{(2\pi)^2 ip_i}\right)\frac{r_0^2}{2}\left[1+\frac{(-\eta+ip_i-ip_icos\theta)r_0}{2}\right.$$

$$\sqrt{\pi}e^{\frac{(-\eta+ip_i-ip_icos\theta)^2r_0^2}{4}}$$

$$\left.erfc\left(-\frac{(-\eta+ip_i-ip_icos\theta)r_0}{2}\right)\right]$$

$$+\frac{V_0}{i}k_e^2\nabla T_{eTi}\nabla T_{eTf}4\pi^2\delta(\omega_{eT})$$

$$cos\theta\, e^{-\frac{a_0^2}{r_0^2}}\frac{\sqrt{\pi}\left(\frac{2}{r_0^2}+\eta^2\right)r_0^5}{4}e^{\frac{\eta^2r_0^2}{4}}$$

Eq. (9) is obtained by putting value of gaussian-screening potential in Eq. (8) and solving by integration with respect to 'r' and 't'. for 't' integrate we used Jacobi–Anger Expansion ($e^{izsin\theta} = \sum_{n=-\infty}^{\infty} J_n(z)e^{in\theta}$) to solve the integration in term of Bessel function.

Also using complementary error function (erfc(x)) is a special function (Gaussian integrals) for 'r' integrate of Eq. (8).

Now arranging the simplifying Eq. (9) we get final expression of T-matrix as shown in Eq. (10),

$$T_{fi} = \left(\frac{V_0r_0^2}{2p(2\pi)^2}\right)\sum_{n=-\infty} J_n(2R)\,e^{-in\gamma}$$

$$\left[1+\frac{\sqrt{\pi}r_0(-\eta+ip-ipcos\theta)}{2}e^{\frac{(-\eta+ip-ipcos\theta)^2r_0^2}{4}}\right. \tag{10}$$

$$\left.erfc\left(-\frac{(-\eta+ip-ipcos\theta)r_0}{2}\right)\right]$$

$$-\frac{V_0k_e\nabla T_{eTi}r_0^2}{2p_f(2\pi)^{7/2}}\sum_{n=-\infty}^{\infty} J_n(R)\,e^{-in\gamma}$$

$$\left[1+\frac{\sqrt{\pi}r_0(-\eta+ip_f-ip_f cos\theta)}{2}\right.$$

$$\left.e^{\frac{(-\eta+ip_f-ip_f cos\theta)^2 r_0^2}{4}} erfc\left(-\frac{\left(-\eta+ip_f-ip_f cos\theta\right)r_0}{2}\right)\right]$$

$$-\frac{V_0 k_e \nabla T_{eTf} r_0^2}{2p_i(2\pi)^{7/2}}\sum_{n=-\infty}^{\infty} J_n(R)\, e^{-in\gamma}$$

$$\left[1+\frac{\sqrt{\pi}r_0(-\eta+ip_i-ip_i cos\theta)}{2}\right.$$

$$e^{\frac{(-\eta+ip_i-ip_i cos\theta)^2 r_0^2}{4}}$$

$$\left.erfc\left(-\frac{(-\eta+ip_i-ip_i cos\theta)r_0}{2}\right)\right]$$

$$+\frac{\sqrt{\pi}V_0 \nabla T_{eTi}\nabla T_{eTf} 2\pi cos\theta k_e^2 r_0^5}{4i}$$

$$\left(\frac{2}{r_0^2}+\eta^2\right)e^{\frac{\eta^2 r_0^2}{4}-\frac{a_0^2}{r_0^2}}$$

Now Eq. (10) is final equation used to calcite the DCS for the study of scattering dynamic of electrons in presence of laser field with gaussian-screening potential. As we know that DCS is directly realted to T-matrix (Kavazović et al., 2021) and realted by Eq. (11) as shown,

$$\frac{d\sigma}{d\Omega}=\frac{K_f}{K_i}\left|T_{fi}\right|^2 \qquad (11)$$

Now putting value of T from (10) in (11) we get DCS. The obtained equation was sued to study the scattering dynamics of electron with gaussian-screening potential in presence of laser in thermal and nonthermal environment.

3. Results and discussion

The developed Eq. (11) was computed using MATLAB programming language with considering different numerical value change in momentum = 0.3 eV, field strength = 1 a.u., photon energy = 1.17 eV, separation distance = 10 Å, and electron conductivity (k_e) = 1 a.u. The result of computed graphs with this numerical value is shown in Figure 1(a), which presents the DCS with scattering angle, for different polarization cases (linear, circular, and elliptical). The results indicate that the DCS for elliptical polarization is highest, followed by circular and then linear. This trend arises due to ellipticity: in elliptical polarization, the electron oscillates with a larger probability of interaction because of the broader geometry, covering a wider interaction region compared to circular. Similarly, circular polarization covers a larger interaction region than linear due to its geometry. The alternating high and low peaks are attributed to resonance effects—higher peaks correspond to resonance with the superposition of multiple photons, while lower peaks arise from resonance with fewer photons. In general, the DCS decreases in amplitude with increasing scattering angle, since oscillation amplitude diminishes with angle. Figure 1(b) shows the variation of DCS with scattering angle under different conditions. Here too, the DCS for elliptical polarization is greater than that of circular and linear. Beyond ~45°, the DCS for elliptical polarization decreases, while circular and linear cases show a decrease only at higher scattering angles. Additionally, the thermal case (around room temperature) shows a higher DCS compared to the non-thermal case (absence of temperature effects), provided no screening effect is present.

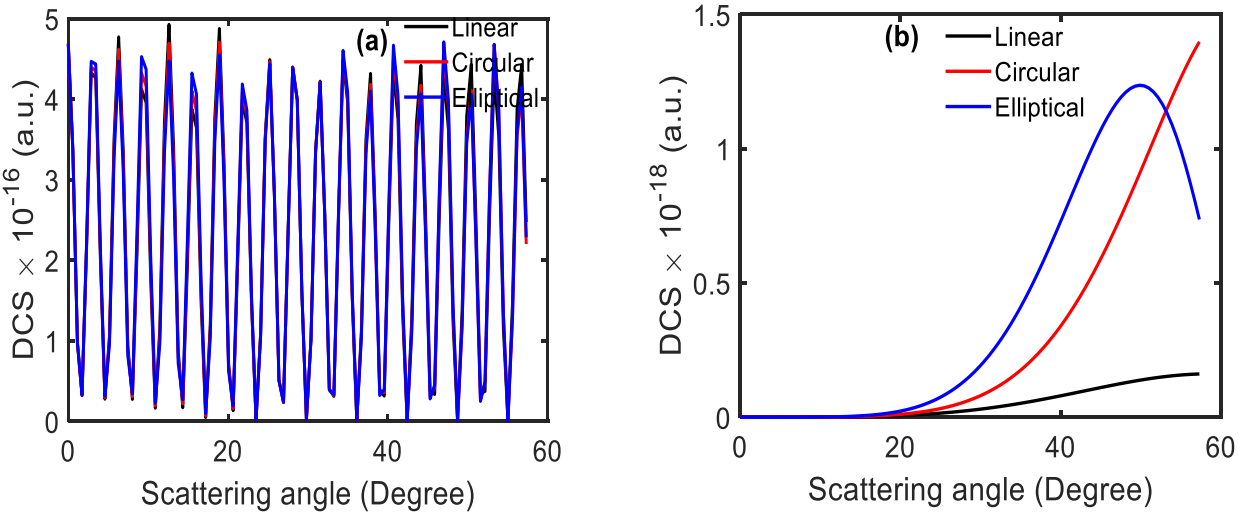

Figure 1. DCS with scattering angle at $\eta = 0$ (a) $\nabla T_{eTi} = 293K$ and $\nabla T_{eTf} = 300K$ (b) $\nabla T_{eTi} = \nabla T_{eTf} = 0K$

Figure 2(a) shows that the DCS increases sharply up to about 20°, after which it decreases. The observed peak is attributed to resonance. Among the polarization cases, the DCS for elliptical polarization is the highest, followed by circular and then linear. Furthermore, Figure 2 illustrates the DCS at different screening parameters. It is observed that with increasing screening parameter values, the DCS also increases. Additionally, higher screening enhances the resonance effect, leading to the appearance of smaller resonances, which are shifted towards smaller scattering angles, as seen in Figures 2(a)–2(d). This indicates that resonance is strongly influenced by the screening parameters. Therefore, by considering screening effects around the potential of the target atom, one can measure and control scattering experiments more effectively. The results, shown in Figure 3 at a scattering angle of 27°, present the DCS variation with momentum change for both thermal and non-thermal cases across all polarization types, without considering screening parameters. In both thermal and non-thermal cases, the DCS for elliptical polarization is greater than that for circular, and circular is higher than linear.

In the thermal case ($\nabla T_{eTi} = 293$ K and $\nabla T_{eTf} = 300$ K), the DCS is significantly higher compared to the non-thermal case ($\nabla T_{eTi} = \nabla T_{eTf} = 0$ K, considered as non-thermal).

Additionally, in the thermal case, the DCS remains nearly constant up to about 4 eV, after which a resonance occurs around 5 eV, resulting in the observed peak in Figure 3(a). When comparing the DCS with Kurmi et al. for laser-assisted quantum dots in the absence of temperature, the DCS is observed to decrease with increasing incident energy, showing a trend similar to the slow decrease presented in Figure 3(b) (Kurmi et al., 2025).

A more detailed comparison was limited, as no additional literature for similar cases could be found. Such resonance does not appear in the non-thermal case. This indicates that temperature plays an important role in laser-assisted scattering and can be used to manipulate both experimental observations and the calculation of higher DCS values.

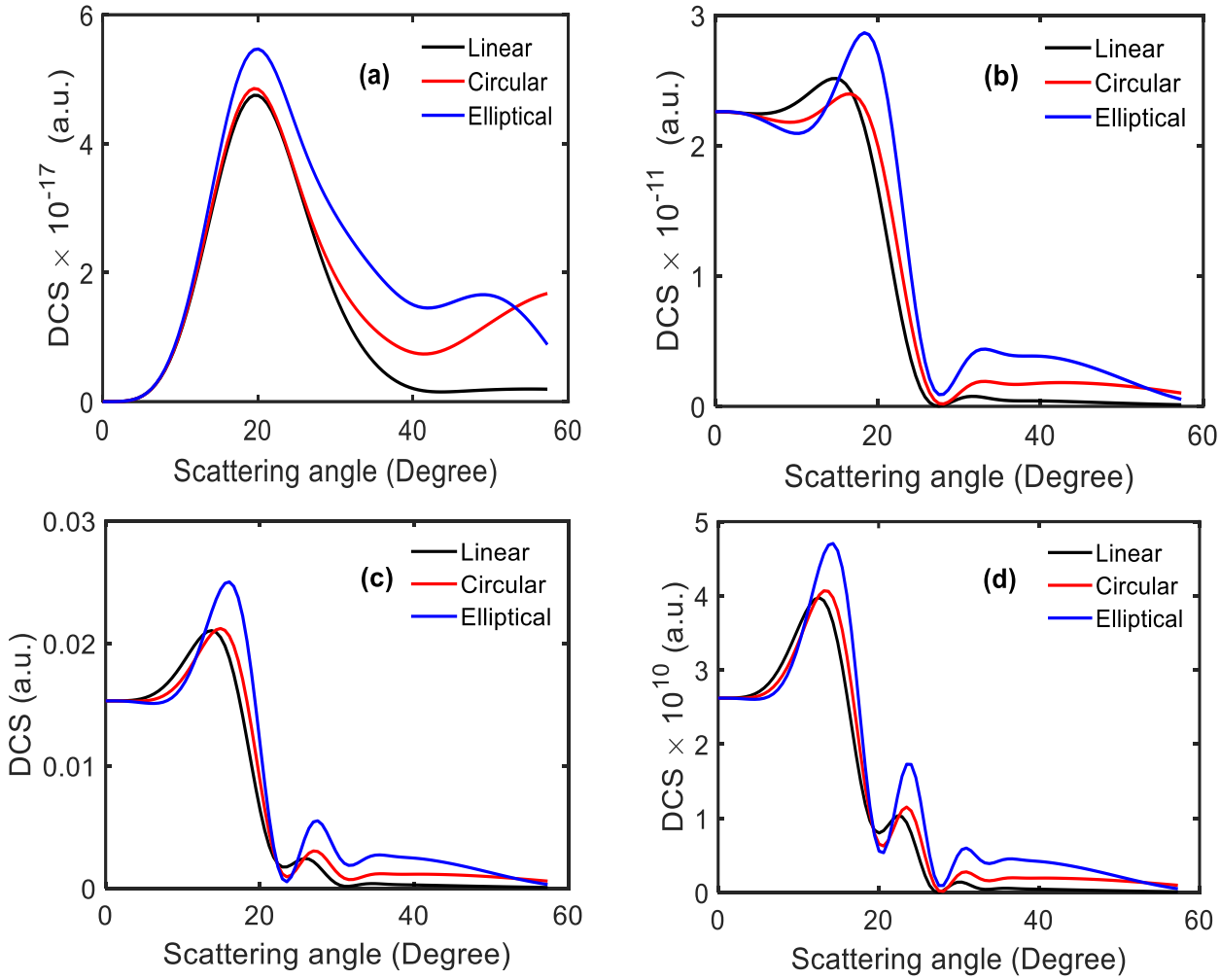

Figure 2. DCS with scattering angle (a) $\eta = 0.2$, (b) $\eta = 0.4$, (c) $\eta = 0.6$ and (d) $\eta = 0.8$ at $q = 0.3\ eV$, $a_0 = 1$, $r_0 = 10$ at at $\nabla T_{eTi} = 293$K and $\nabla T_{eTf} = 300$K

10.57647/jtap.2026.8615.0306

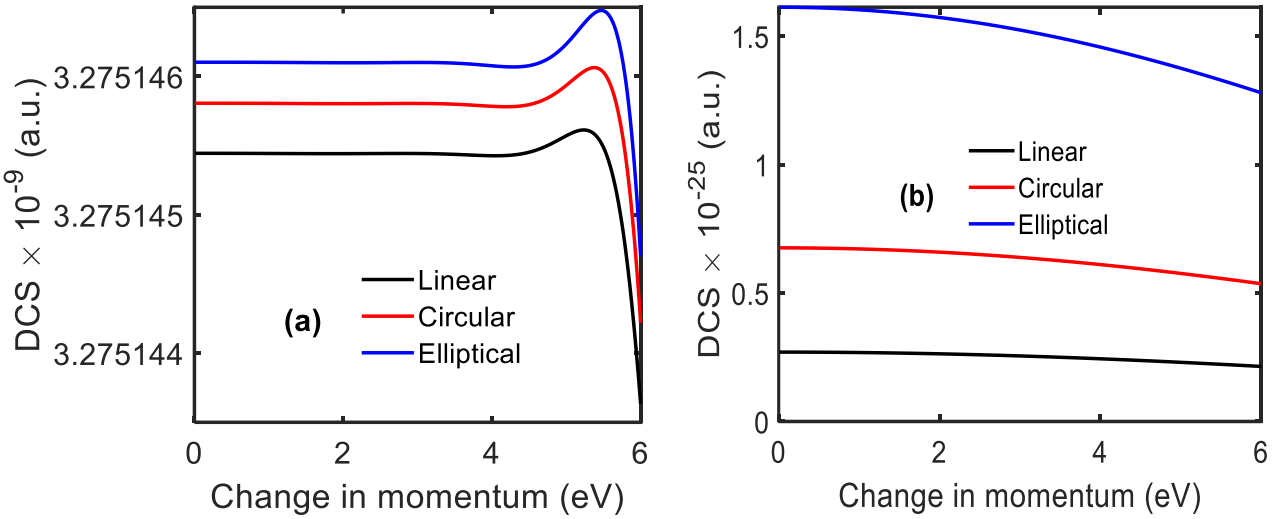

Figure 3. DCS with change in momentum at $\eta = 0$(a) $\nabla T_{eTi} = 293$ K and $\nabla T_{eTf} = 300$ K, (b) $\nabla T_{eTi} = \nabla T_{eTf} = 0$ K

Figures 4(a) and 4(b) show the DCS as a function of momentum change at a lower scattering angle of 5.7°, considering different screening parameters in the thermal case, while Figures 4(c) and 4(d) show the corresponding results at 27°. At 5.7°, the DCS decreases sharply in the low-energy region due to electron transformation into the target and the surrounding scattering environment. With increasing screening parameters, the DCS tends to converge, as shown in Figure 4(b), maintaining a similar trend to that observed for lower screening values. At the higher scattering angle of 27°, the DCS for smaller screening parameters is found to be lower than that for larger screening parameters. Resonance is observed at 27°, whereas weaker resonances appear at 5.7°. The nearly constant DCS in the range of ~0.5–4 eV corresponds to the condition where the electrostatic interaction energy is approximately equal to the resonance energy, as depicted in Figure 4. Figure 5 presents the DCS as a function of distance separation for both thermal and non-thermal cases without considering screening effects. The results show that the DCS in the thermal case is higher and exhibits an opposite trend compared to the non-thermal case, as illustrated in Figures 5(a) and 5(b), respectively. In the thermal case (Figure 5a), the DCS values for nearly all polarization states are almost equal. This indicates that thermal effects dominate over polarization geometry, meaning that at finite temperature the oscillation region becomes uniform across different polarizations. This conclusion is further supported by the contrasting behavior observed in the non-thermal case (Figure 5b). Figure 6 presents the DCS as a function of distance separation, considering both thermal and screening effects, for elliptical polarization cases. At lower screening values, the DCS behavior is similar to the thermal case without screening (as shown previously in Figure 5a). However, at higher screening values, the DCS exhibits two distinct behaviors. For distances below ~1.5 Å, the DCS follows the same trend as in the low-screening case. Between ~1.5 Å and 4.5 Å, the DCS remains nearly constant, indicating that in this region the electrostatic interaction energy equals the rest energy of the interacting particles (Figure 6b). Beyond 4.5 Å, the DCS increases with distance, resembling the behavior observed in the non-thermal case (Figure 5b). The general nature of the DCS under screening is similar across other two polarization cases (circular and linear).

Figure 7 shows the variation of DCS with photon energy for both thermal and non-thermal cases. Figures 7(a) and 7(b) correspond to the thermal and non-thermal cases, respectively. In the thermal case (Figure 7a), multiple resonances are observed. The smaller DCS peaks correspond to resonances involving the superposition of a lower number of interacting particles, whereas the larger peaks arise from resonances with the superposition of a greater number of particles in the scattering process. Around 0.5 eV, the DCS decreases for all polarization states. At lower photon energies, the DCS for elliptical polarization is highest, followed by circular and then linear. However, with increasing photon energy, this order reverses: the DCS for linear polarization becomes higher than circular, and circular becomes higher than elliptical. This behavior is attributed to thermal effects being dominant at lower photon energies. In the non-thermal case (Figure 7b), the DCS maintains the expected ordering—elliptical > circular > linear. Only small resonance peaks are observed: the first (below 0.2 eV) is due to resonance with the superposition of fewer scattering particles, while the second (0.2–0.5 eV) corresponds to resonance with a larger number of scattering particles. Beyond 0.9 eV, the DCS increases exponentially, as shown in Figure 7(b).

10.57647/jtap.2026.8615.0306

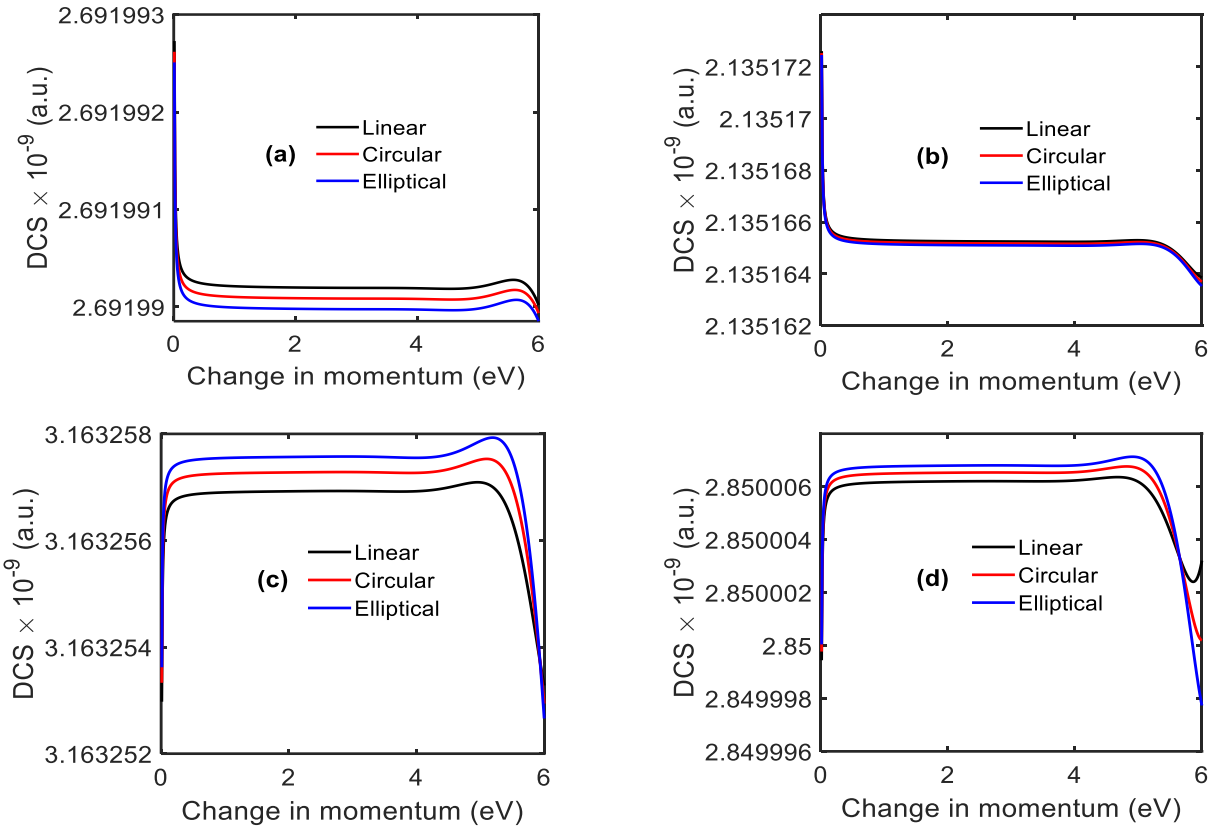

Figure 4. DCS with change in momentum (a) $\eta = 0.2$ at 5.7°, (b) $\eta = 0.8$ at 5.7°, (c)) $\eta = 0.3$ at 27° and (d)) $\eta = 6$ at 27 °

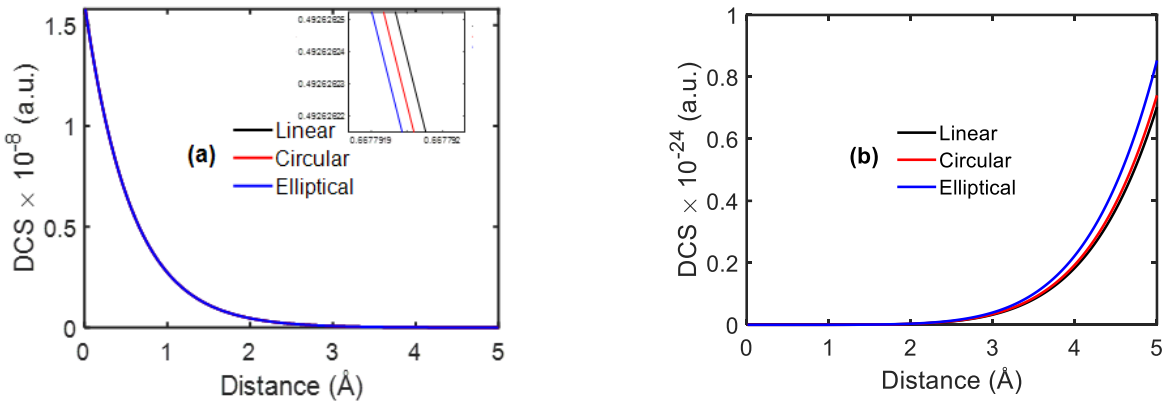

Figure 5. DCS with distance separation at $\eta = 0$(a) $\nabla T_{eTi} = 293$ K and $\nabla T_{eTf} = 300$ K, (b) $\nabla T_{eTi} = \nabla T_{eTf} = 0$ K

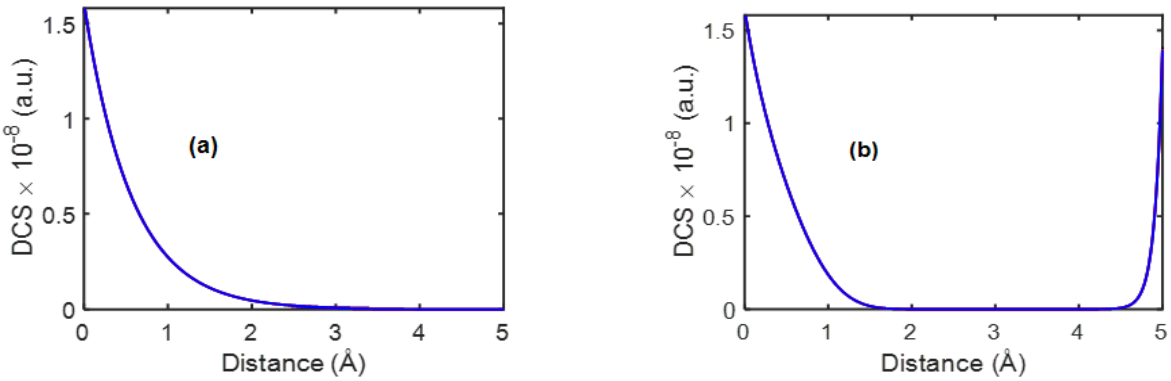

Figure 6. DCS with distance separation (a) $\eta = 0.1$, (b) $\eta = 1$ at $\nabla T_{eTi} = 293$ K and $\nabla T_{eTf} = 300$ K

10.57647/jtap.2026.8615.0306

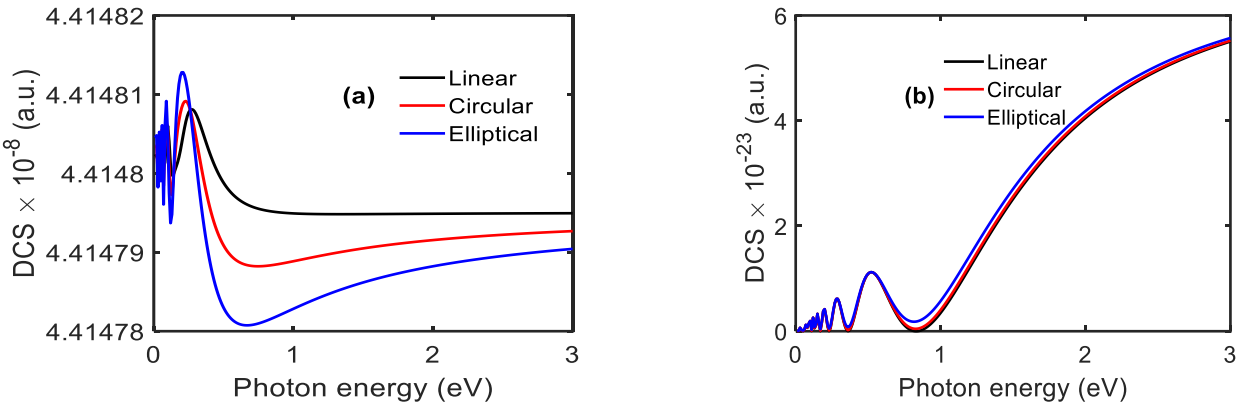

Figure 7. DCS with photon energy at η=0.1 (a) $\nabla T_{eTi} = 293K$ and $\nabla T_{eTf} = 300K$, (b) $\nabla T_{eTi} = \nabla T_{eTf} = 0K$

Figure 8 presents the DCS at both small (5.7°) and larger (27°) scattering angles for the thermal case. Figures 8(a) and 8(b) demonstrate that the DCS is strongly influenced by the scattering angle.

At the smaller angle (Figure 8a), the resonance peak is sharp, which indicates that resonance and superposition coincide, thereby amplifying the amplitude. At the larger angle (Figure 8b), the peak becomes flatter, suggesting that resonance and superposition do not coincide.

A similar behavior of DCS is observed under higher screening conditions for both thermal and non-thermal cases.

At higher photon energies, the DCS becomes nearly constant, implying that at such energies the electrostatic interaction energy equals the rest energy, preventing the projectile and target from approaching each other more closely.

For energies below 0.5 eV (Figure 8a), the DCS follows the order elliptical > circular > linear. However, above 0.5 eV, the trend reverses, with linear > circular > elliptical.

This highlights the important roles of screening, temperature, and scattering angle in determining the behavior of projectile–target interactions. For the larger scattering angle (Figure 8b), the general polarization ordering is maintained: elliptical > circular > linear.

Figure 9 is computed using a change in momentum of 0.3 eV, a scattering angle of 5.7°, a field strength of 0.1 a.u., a photon energy of 1.17 eV, a separation distance of 1 Å, and 10 photon exchanges during scattering.

The Figure 9 shows the DCS as a function of the screening effect for elliptical polarization, revealing a nearly similar trend across other two polarization cases.

The results indicate that the DCS increases exponentially with the screening effect for all polarization case (elliptical, circular, and linear).

In addition, the work has limitations in comparing the findings with previous studies, as the DCS in similar fields has not been extensively investigated either experimentally or theoretically.

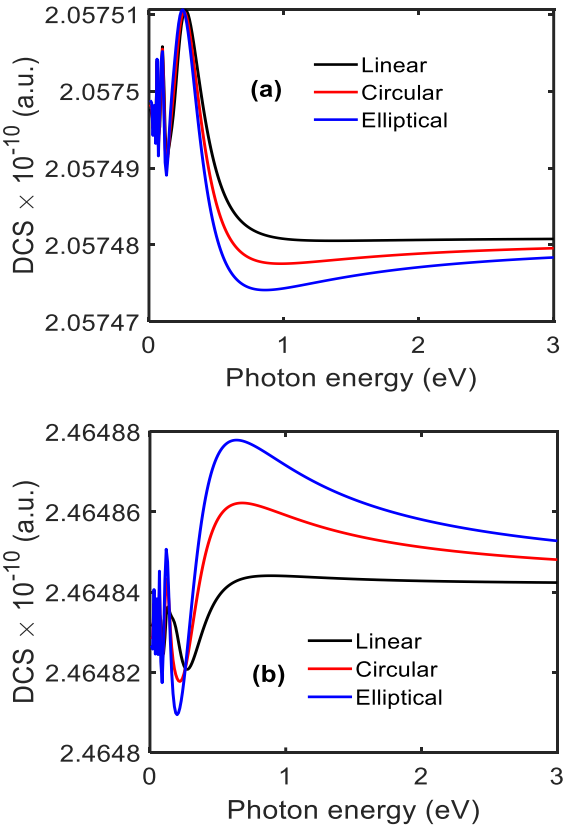

Figure 8. DCS with photon energy at $\eta = 0.4$ (a) 5.7 degree and (b) 27.0 degre with $\nabla T_{eTi} = 293$ K at $\nabla T_{eTf} = 300K$

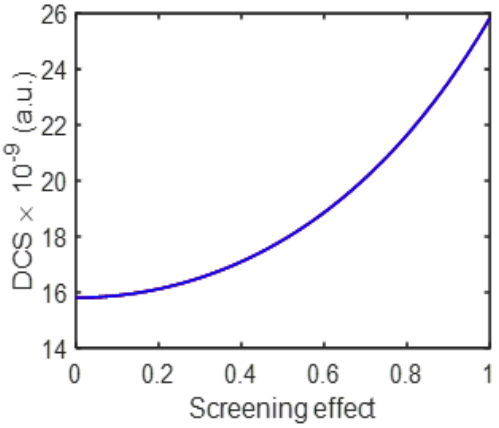

Figure 9. DCS with screening effect

4. Conclusion

The present study provides a detailed analysis of the differential cross-section (DCS) under varying physical conditions such as scattering angle, momentum change, photon energy, screening effects, and thermal contributions.

Across all cases, polarization plays a central role, with elliptical polarization consistently exhibiting the highest DCS values, followed by circular and linear. Temperature is shown to significantly enhance scattering, producing sharper resonances and higher amplitudes compared to non-thermal conditions. Screening parameters strongly influence resonance behavior, shifting peaks toward smaller angles and increasing DCS values at higher strengths. Distance separation further reveals contrasting behaviors between thermal and non-thermal regimes, while photon energy introduces notable polarization reversals at higher values.

Scattering angle also critically modifies resonance sharpness, with smaller angles amplifying resonance effects. The tunability of DCS in laser-assisted scattering has practical significance in real systems, such as optimizing quantum dot lasers for photonic and communication devices, enhancing quantum information processing through controlled exciton states, and improving biomedical imaging and therapy by tailoring QD–laser interactions.

Acknowledgement

We would like to thank all faculties members of department of physics, patan multiple campus, Tribhuvan university for provide peaceful environment during this research.

Funding sources

No funding for this research.

Ethical consideration

Since it is theoretical work so no any living organism is used in this experiment.

Authors Contribution

Dolraj Paudel prepared the original draft and methodology, while Saddam Husain Dhobi identified the problem, designed the methodology, and performed the coding. Others contributed by reviewing and validating the work.

Availability of data and materials

No data are used, code are generated for developed equation and provided by corresponding authors in request.

Conflict of interests

No conflict of interest

References

Bahar, M. K., & Soylu, A. (2018). Laser-driven two-electron quantum dot in plasmas. *Physics of Plasmas, 25*(6), 062113. doi:10.1063/1.5028325.

Bauer, D. (2006). Theory of intense laser-matter interaction. Max-Planck-Institut für Kernphysik.

Bransden, B. H., & Joachain, C. J. (2003). *Physics of Atoms and Molecules* (2nd ed.). Prentice Hall, Harlow, England.

Bryant, G. W. (1987). Electronic structure of ultrasmall quantum-well boxes. *Physical Review Letters, 59*(11), 1140.

Chakraborty, T. (1999). *Quantum Dots* (1st ed.). Elsevier Sciences.

Dhobi, S. H., Gupta, S. P., Yadav, K., Nakarmi, J. J., & Jha, A. K. (2024). Differential cross section with Volkov-thermal wave function in Coulomb potential. *Atom Indonesia, 50*(1), 19-25. https://doi.org/10.55981/aij.2024.1309

Dhobi, S. H., Yadav, K., Gupta, S. P., Nakarmi, J. J., & Jha, A. K. (2025). Non-monochromatic laser assist scattering in thermal environment. *Journal of the Nigerian Society of Physical Sciences, 7*, 2345. https://doi.org/10.46481/jnsps.2025.2345

Durak, S. (2016). Laser field effect on the nonlinear optical properties of quantum dots. (Doctoral dissertation, Dokuz Eylül University Graduate School of Natural and Applied Sciences).

Durak, S., & Sakiroglu, S. (2023). Theoretical investigation of laser field effect on nonlinear optical properties of quantum dots. *Physica B: Condensed Matter, 650*, 414575. https://doi.org/10.1016/j.physb.2022.414575

González De La Cruz, G., & Gurevich, Y. G. (1996). Electron and phonon thermal waves in semiconductors: An application to photothermal effects. *Journal of Applied Physics, 80*(3), 1726-1730. https://doi.org/10.1063/1.362971

Gunatilaka, C. C., & Gamalath, K. A. I. L. W. (2016). Electron dynamics in a strong laser field with Gaussian potential well. *World Scientific News, 40*, 265-284.

Jacob, R., Winnerl, S., Fehrenbacher, M., Bhattacharyya, J., Schneider, H., Wenzel, M. T., Helm, M. (2012). Intersublevel spectroscopy on single InAs-quantum dots by terahertz near-field microscopy. *Nano Letters, 12*(8), 4336–4340.

doi:10.1021/nl302078w

Kavazović, K., Čerkić, A., & Milošević, D. B. (2021). Electron-molecule scattering in a bichromatic elliptically polarised laser field: Plateau structures and two-centre interference minima. *Molecular Physics, 119*(14), e1948123.

Kim, B. N. (2022). Angular Distribution of Electron-Helium Scattering in the Presence of A 1.17 eV Laser Field, Theses and Dissertations--Physics and Astronomy, 95. https://uknowledge.uky.edu/physastron_etds/95

Khordad, R. (2012). Pressure effect on optical properties of modified Gaussian quantum dot. *Physica B, 407*, 1128–1133.

Kroll, N. M., & Watson, K. M. (1973). Charged-particle scattering in the presence of a strong electromagnetic wave. *Physical Review A, 8*, 804–809.

Kurmi, R. P., Yadav, K., Shrestha, A., & Dhobi, S. H. (2025). Laser assist quantum dot scattering with Gaussian potential. *Physics Open, 23*, 100267. https://doi.org/10.1016/j.physo.2025.100267

Li, L., Qian, H., & Ren, J. (2005). Article in chemical communications. Cambridge, United Kingdom: pubs.rsc.org. doi:10.1039/b412686f

Liu, P., Wang, Q., & Li, X. (2009). Studies on CdSe/L-cysteine quantum dots synthesized in aqueous solution for biological labeling. *Journal of Physical Chemistry C, 113*(18), 7670–7676.

doi:10.1021/jp901292q

Nikolopoulos, L. A. A., & Bachau, H. (2016). Theory of photoionization of two-electron quantum dots in the resonance region in THz and mid-IR fields. *Physical Review A, 94*(5), 053409. doi:10.1103/PhysRevA.94.053409

Peeters, F. M. (1990). Magneto-optics in parabolic quantum dots. *Physical Review B, 42*(2), 1486(R).

Ungan, F., Bahar, M. K., Barseghyan, M. G., Pérez, L. M., & Laroze, D. (2021). Effect of intense laser and electric fields on nonlinear optical properties of cylindrical quantum dot with Morse potential. *Optik, 236*, 166621. doi:10.1016/j.ijleo.2021.166621

Xie, W. (2008). Nonlinear optical properties of a hydrogenic donor quantum dot. *Physics Letters A, 372*, 5498–5500.

Yu, B., Zhu, C., & Gan, F. (2000). Nonlinear optical absorption and refraction by CdTe microcrystals doped in glass. *Journal of Applied Physics, 87*(4), 1759–1761. doi:10.1063/1.372088

Yadav, K., Gupta, S. P., & Nakarmi, J. J. (2020). Elliptically polarized laser assisted elastic electron-hydrogen atom collision and differential scattering cross-section. *Himalayan Physics, 9*, 93–102.

Zou, W., Qiao, J., Hu, X., Ge, X., & Lian, H. (2011). Synthesis in aqueous solution and characterization of a new cobalt-doped ZnS quantum dot as a hybrid ratiometric chemosensor. *Analytica Chimica Acta, 708*(1–2), 134–140. doi:10.1016/j.aca.2011.09.044